Correction methods for shadow-band diffuse irradiance measurements: assessing the impact of local adaptation

J. M. Rodríguez-Muñoz*, A. Monetta, R. Alonso-Suárez, I. Bove, G. Abal

Laboratorio de Energía Solar, Universidad de la República,
Av. L. Batlle Berres km 508, Salto, Uruguay

Abstract

Shadow-bands are a low cost alternative when a precision solar tracker is not available. Adequate precision may be achieved if the measured diffuse irradiance is corrected to account for the sky portion blocked by the shadow-band. The isotropic sky assumption leads to a systematic under estimation of diffuse irradiance. Several correction methods have been proposed to take into account the anisotropic effects. However, their performance at a given site depends on the dominant local climate. In this work, it is shown that the local adaptation of shadow band correction methods results in a significant improvement in the diffuse irradiance measurement's accuracy. Nine well-known correction methods are implemented and tested (both in their original and locally adapted versions) for the Pampa Húmeda region of southeastern South America. In absence of local adaptation, only one of the pre-existing methods improves the simple isotropic model. All locally adapted versions perform similarly well and outperform significantly the original methods. A new model based on the parametrization of Battle's model is proposed. It provides the best performance compared to all locally adapted pre-existing models, under all-sky and discriminated sky conditions.

Keywords: diffuse irradiance, shadow-band measurement, corrections models, sky anisotropy.

1. Introduction

Diffuse radiation represents a significant part of the Sun's radiation that reaches ground level. In mid-latitude temperate climates about 1/3 of the annual global horizontal irradiation is diffuse (Abal et al., 2017). This part of global irradiance has an important role in modeling the solar energy yield of various solar technologies. It is required in transposition models to estimate the global irradiance on inclined surfaces, the relevant solar input for solar photovoltaic and several thermal applications. Furthermore, knowledge of the global and diffuse irradiances incident on a surface can be used to estimate the Direct Normal Irradiance (DNI), relevant for concentrated solar systems, via the closure relation (Eq. (1)), when measurements of this

*Corresp. author: J. M. Rodríguez-Muñoz, jrodrigue@fing.edu.uy

List of Symbols

δ	Solar declination angle.
ϵ	Sky clearness index (Perez et al., 1990).
ω	Solar hour angle.
ω_s	Sunset solar hour angle.
ϕ	Local latitude angle.
τ_b	Beam transmittance, G_b/G_0.
θ	Zenith or polar angle of sky element.
θ_0	Angle subtended by the shadow-band.
θ_z	Solar zenith angle.
φ	Azimuth angle of sky element.
φ_s	Solar azimuth angle.
b_i	Anisotropy parameters of the Muneer & Zhang model, for $i = 1, 2$.
$d\Omega$	Solid angle for a sky element, $\sin\theta\, d\theta\, d\varphi$.
f	Correction factor for diffuse horizontal irradiance, such that $G_{dc} = f\, G_{du}$.
f_d	Diffuse fraction, G_d/G_h.
G_0	Extraterrestrial solar irradiance (modulated by the orbital factor).
G_b	Direct normal irradiance, Wm^{-2}.
G_d	Diffuse horizontal irradiance, Wm^{-2}.
G_h	Global horizontal irradiance, Wm^{-2}.
G_{0h}	Extraterrestrial horizontal irradiance, $G_0 \cos\theta_z$.
G_{dc}	Corrected diffuse horizontal irradiance, Wm^{-2}.
G_{di}	Diffuse horizontal irradiance intercepted by a shadow-band, Wm^{-2}.
G_{du}	Uncorrected diffuse horizontal irradiance, as measured by a shaded pyranometer, Wm^{-2}.
k_d	Diffuse clearness index, G_d/G_{0h}.
k_t	Clearness index, G_h/G_{0h}.
L_p	Sky angular radiance, Wm^{-2}/str.
N	Sunshine duration (fractional hours).
N_0	Maximum sunshine duration for a given site and day (fractional hours).
n_r	Relative sunshine duration, N/N_0.
r	Shadow-band radius, m.
S	Fraction of diffuse horizontal irradiance intercepted by a shadow-band, G_{di}/G_d.
w	Shadow-band width, m.

component are not available. For a horizontal surface, it can be stated that

$$G_h = G_b \cos\theta_z + G_d, \tag{1}$$

where θ_z is the solar zenith angle (see the list of symbols for the other definitions). The DNI estimated from this expression can have high uncertainties, specially at low Sun elevations. If no diffuse irradiance measurements are available at a given site, a separation model can be used to estimate the diffuse fraction from normalized global irradiance and other variables (Ridley et al., 2010; Ruiz-Arias et al., 2010; Gueymard & Ruiz-Arias, 2016), at the expense of adding considerable uncertainty even if the separation models are locally adjusted to high-quality data (Abal et al., 2017).

To measure diffuse radiation, beam irradiance must be blocked from the sensor by a shadowing device. This can be done in several forms: a shadow-sphere mounted on a precision solar tracker, a manually adjusted shadow-band, an automatically driven rotating shadow-band (RSR systems) or by a specifically designed fixed shadow-mask with no moving parts (Badosa et al., 2014), among other alternatives. These methods have different accuracy, cost and maintenance requirements (Vignola et al., 2019). The shadow-sphere is the low uncertainty option when a precision solar tracker is available. A shadow-band is a low-cost alternative which can be potentially accurate if appropriate correction factors are used and it is a frequent choice due to its good balance between cost, maintenance and accuracy.

During a diffuse irradiance measurement, the shadow-band blocks the direct beam from the pyranometer but also shades incoming diffuse irradiance from part of the sky dome. A correction factor, $f = G_d/G_{du}$, must be applied to the uncorrected measurement, $G_{du} = G_d - G_{di}$, in order to account for the blocked diffuse irradiance. The irradiance intercepted by the band, G_{di}, depends on the shadow-band geometry and the diffuse radiance distribution in the sky, which is affected by the cloud's distribution. The correction factor is usually expressed as

$$f = \frac{1}{1-S}, \tag{2}$$

in terms of the fraction of blocked diffuse irradiance, $S = G_{di}/G_d$. The simplest expression for S is obtained by assuming an isotropic distribution of the diffuse radiance in the sky. This calculation was originally done by Drummond (1956) and it results in a correction factor that depends on the geometry of the shadow-band, the solar declination angle and the latitude of the observer. However, the isotropic assumption is known to be inaccurate: Drummond realized that due to anisotropy effects in the sky this correction factor would underestimate the diffuse irradiance and suggested to increment its monthly mean value by 3 to 7% of the measurements average, depending on the predominant cloudiness conditions. Higher underestimations have been reported, for instance, Stanhill (1985) found underestimations between 11 and 27% by working with hourly data from the region of the Dead Sea. Under clear-sky conditions, most anisotropy in the sky radiance distribution comes from the bright circumsolar region. In the presence of clouds, multiple reflection and scattering can produce more complex anisotropy effects which should be taken into account in order to obtain accurate correction factors.

Several sophisticated models that attempt to improve on the isotropic assumption have been proposed. Two broad approaches can be distinguished: (i) proposals based on analytical sky radiance distributions, from which the blocked incident diffuse irradiance can be numerically integrated (Ineichen et al., 1984; Rawlins & Readings, 1986; Siren, 1987; Vartiainen, 1999; Muneer & Zhang, 2001) and (ii) proposals based on empirical methods attempting to model directly a correction factor (Painter, 1981; Kasten et al., 1983; Steven, 1984; LeBaron et al., 1990; Kudish & Ianetz, 1993; Batlles et al., 1995). Several authors have evaluated the accuracy of different correction methods working with data from different climates (Rawlins & Readings, 1986; Batlles et al., 1995; López et al., 2004; Kudish & Evseev, 2008; Sánchez et al., 2012). However, there is no broad consensus as to which is the best correction method and this is to be expected, since the local climate is known to be important in the related diffuse-direct separation problem and there is no universal separation model (Gueymard & Ruiz-Arias, 2016).

The main objectives of this work are to implement and evaluate nine pre-existing diffuse irradiance correction models and to propose an enhanced correction model, that is optimized for the Pampa Húmeda region. This is a broad area of low homogeneous grasslands in southern South America, including the southern part of Brazil, the eastern part of Argentina and the territory of Uruguay. The climate is temperate, classified as Cfa in the updated Köpen-Geiger scheme (Peel et al., 2007). The models are evaluated both in their original (generic) versions and in locally-adjusted or site-adapted forms working with 5-minute time intervals, in order to include some transient effects. Different types of models are considered, including the isotropic correction, sky radiance based models and phenomenological models. Without local data and studies it is difficult to establish general recommendations for a given site, either for original or locally-adapted models, being this an issue that has not been covered previously in the literature for these kinds of correction models. The evaluation of the generic form of the models is done to identify the best generic method and to quantify the impact of local adaptation in our region's climate. Full information is provided to enable the use of locally adjusted or adapted models in the Pampa Húmeda or in similar temperate climate regions. A new optimized model, which outperforms the pre-existing locally adapted models in this region, is presented. The model is an enhancement of the pre-existing Batlles et al. method, replacing the former sky clearness index for a modified version which takes into account the solar altitude, and achieving a lower bias and dispersion by considering in its formulation an additional independent term and the bins of the Perez et al. (1993) model. In fact, the new proposal achieves lower bias and dispersion, not only under all-sky conditions, but also when discriminated for clear sky, partly cloudy and overcast skies. The comparison shows that the performance of some phenomenological models critically depends on the local adaptation and some sophisticated sky radiance models do not provide a significant performance improvement over the simple isotropic model. Finally, as a contribution on the theoretical side, it is shown that Kasten's equation, used to transfer correction factors between different shadow-band geometries (originally derived for a isotropic sky), is valid for any sky radiance distribution, provided the shadow-band satisfies certain requirements.

This article is organized as follows. In Section 2 the details of the selected correction models are described, including the novel proposal of this work. In Section 3 the data being used is discussed along with the quality filters applied. Section 4 describes the implementation and local adaptation of the models and Section 5 discusses their performance. Finally, in Section 6 the main conclusions are summarized.

2. Shadow-band correction models

Most shadow-band correction models either parametrize the correction factor f or estimate the fraction of diffuse irradiance intercepted by the band, S, to obtain f from Eq. (2). Since $S < 1$ the correction factor will satisfy $f > 1$. This excludes the possibility that the shadow-band increases the diffuse irradiance on the target pyranometer due to reflexion of circumsolar radiation on the internal band surface. Commercial shadow-bands are usually coated with low-reflectivity black paint to minimize this effect. In this article, we assume that this effect can be neglected and $f \geq 1$.

2.1. General considerations on shadow-band correction factors

2.1.1. Geometrical aspects

The sky angular radiance, $L_p(\theta, \varphi)$, describes the flux of radiant energy per unit solid angle incoming from each sky direction (θ, φ) excluding the direct beam. So that the diffuse irradiance reaching an exposed horizontal sensor is

$$G_d = \int_{-\pi}^{\pi} \int_{0}^{\pi/2} L_p(\theta, \varphi) \, \cos\theta \, d\Omega, \tag{3}$$

with $d\Omega = \sin\theta \, d\theta \, d\varphi$. If the sky radiance is isotropically distributed its value is $L_p^{iso} = G_d/\pi$. An expression for the diffuse irradiance intercepted by the band can be obtained by restricting the integration above to the portion of sky blocked by the shadow-band,

$$G_{di} = \iint_{band} L_p(\theta, \varphi) \, \cos\theta \, d\Omega, \tag{4}$$

where the geometry of the shadow-band defines the integration limits. If the ratio between the band width and its radius is small, $b/r \lesssim 0.2$, the surface integral in Eq. (4) can be approximated by a line-integral along the solar path, using the solar hour angle (ω) as the single variable (Steven & Unsworth, 1980):

$$G_{di} = \theta_0 \cos\delta \int_{-\omega_s}^{\omega_s} L_p(\theta_z, \varphi_s) \, \cos\theta_z \, d\omega, \tag{5}$$

where θ_0 is the angle (radians) subtended by the shadow-band as seen by the pyranometer, φ_s is the solar azimuth and δ is the solar declination. Both solar angles, θ_z and φ_s, depend on the solar declination, the site's latitude (ϕ) and w by the usual expressions describing the solar apparent motion (Iqbal, 1983). The integration limits are defined by the extreme values of the hour angle, which for a horizontal surface are $\omega_s = \pm \arccos(-\tan\phi \, \tan\delta)$. In Eq. (5), the geometry of the shadow-band is expressed by θ_0 and is separated from the influence of the sky condition (the line integral). For a flat shadow-band of negligible thickness,

$$\theta_0 = \frac{b}{r} \cos^2\delta. \tag{6}$$

In order to reduce the seasonal dependence of the correction factor, some commercial shadow-bands use a 'U'-shaped profile. For these bands, $\theta_0 \simeq b/r$ (de Simón-Martín et al., 2016) with an error of less than 2% and an impact of less than 0.5% in the correction factor (Kipp & Zonen , 2004).

2.1.2. Drummond's isotropic model (DR)

As mentioned in the introduction, Drummond used the isotropic assumption to evaluate Eq. (5) analytically (Drummond, 1956; Kipp & Zonen , 2004) and obtained

$$S_0 = \frac{2\theta_0}{\pi} \cos\delta \, I_1, \tag{7}$$

where

$$I_1 = \frac{1}{2}\int_{-\omega_s}^{\omega_s} \cos\theta_z \, d\omega = \cos\phi\cos\delta\sin\omega_s + \omega_s \sin\phi\sin\delta, \tag{8}$$

with θ_0 and ω_s expressed in radians (the notation I_1 follows the work of Muneer & Zhang (2001), Subsection 2.2.1). The isotropic correction factor from Eq. (2) is

$$f_0 = \frac{1}{1-S_0} = \left(1 - \frac{2\theta_0}{\pi}\cos\delta\, I_1\right)^{-1} \tag{9}$$

and it depends on the local latitude, day of year and the geometry of the shadow-band, through θ_0. The dependence of f_0 with the day of year for a given latitude and two shadow-band profiles is shown in Fig. 1. Since this expression does not account for anisotropic effects, such as circumsolar radiation, its utilization leads to a systematic underestimation of the diffuse irradiance, except under complete cloud cover when the isotropic approximation is closely satisfied.

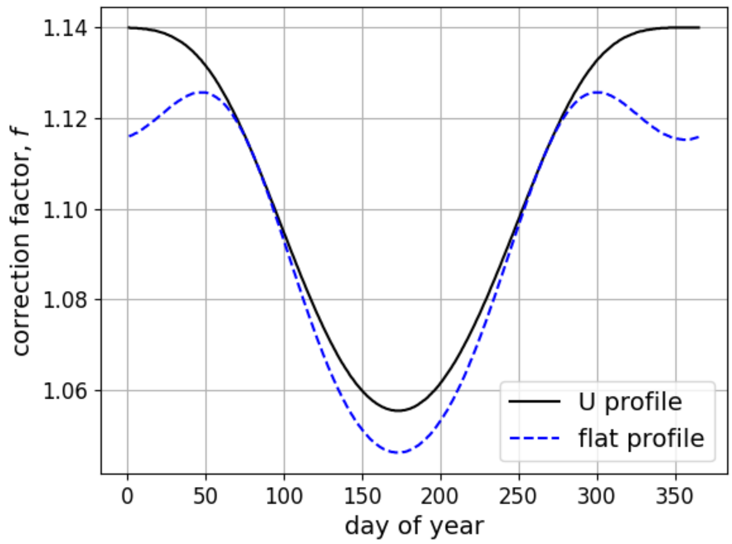

Figure 1: Isotropic correction factor, Eq. (9), for each ordinal day. Latitude is $\phi = -31.28°$ and $b/r = 0.185$.

2.1.3. Transfer of the correction factor to other shadow-bands

The fraction of intercepted diffuse irradiance, Eq. (5), can be written as

$$S = \frac{G_{di}}{G_d} = \theta_0\, \Gamma, \tag{10}$$

where only θ_0 depends on the shadow-band geometry (assumed to satisfy $\theta_0 \lesssim 0.2$) and Γ depends on sky condition and on the Sun's apparent position. It follows that two bands with different geometries, θ_1 and θ_2, will intercept fractions that satisfy $S_1/S_2 = \theta_1/\theta_2$ and the corresponding correction factors will be related by

$$f_2 = \frac{f_1\theta_1}{f_1\theta_1 + (1 - f_1)\,\theta_2}. \tag{11}$$

This useful expression was originally derived by Kasten et al. (1983) for the particular case of isotropic diffuse sky radiance. However, as shown here, it holds valid for an arbitrary sky radiance distribution, provided that two simple conditions are met:

i) Both geometries satisfy $\theta_{1,2} \lesssim 0.20$, so that the approximation in Eq. (5) holds.

ii) That internally reflected diffuse irradiance can be neglected so that Eq. (2) holds and $f \geq 1$.

2.2. Correction models based on assumed sky radiance parametric distributions

2.2.1. Muneer and Zhang (MZ)

As a compromise between a realistic anisotropic distribution and a simplified analytical description that takes into account some anisotropic effects, Muneer & Zhang (2001) use the simple sky radiance distribution from Moon & Spencer (1942),

$$L_p(\theta,\varphi) = L_z \frac{1 + b_i \cos\theta}{1 + b_i}, \tag{12}$$

where L_z is the sky radiance at the zenith ($\theta = 0$) and b_i is a sky radiance distribution index. The index $i = 1, 2$ corresponds to the two half-hemispheres of the sky, depending on the Sun's position. The Sun's half-hemisphere ($i = 1$) is treated separately from the other half-hemisphere ($i = 2$). The original Moon & Spencer proposal is a sky radiance distribution model for overcast sky and Muneer & Zhang extended it to all-sky conditions by introducing a clearness index ($k_t = G_h/G_{0h}$) dependence in the b_i parameters. This parametrization was originally proposed by Muneer (1990) as part of a transport model relating the diffuse irradiance on an inclined surface to the horizontal diffuse irradiance. The relationships between b_i and k_t were fitted by Muneer using data of horizontal and inclined diffuse irradiance from one site to adjust the coefficients and from two sites to validate the model. For cloudy conditions ($k_t \leq 0.2$), $b_1 = b_2 = 1.68$. For other sky conditions ($k_t > 0.2$),

$$b_1 = \frac{3.6 - 10.46\,k_t}{-0.4 + 6.974\,k_t} \qquad \text{and} \qquad b_2 = \frac{1.565 - 0.990\,k_t}{0.957 + 0.660\,k_t}. \tag{13}$$

The integrals in Eqs. (3) and (5) can be evaluated analytically using the radiance distribution from Eq. (12), resulting in expressions for G_d and G_{di},

$$G_d = \frac{\pi L_z}{6}\left[\frac{3 + 2b_1}{1 + b_1} + \frac{3 + 2b_2}{1 + b_2}\right] \tag{14}$$

$$G_{di} = 2\theta_0 \cos\delta\, L_z \left[\frac{I_1 + I_2\, b_1}{1 + b_1}\right], \tag{15}$$

where I_1 is given by Eq. (8) and

$$I_2 = \omega_s \sin^2\phi \sin^2\delta + \frac{\sin\omega_s \sin(2\phi)\sin(2\delta)}{2} + \frac{\cos^2\phi\,\cos^2\delta}{2}\left[\omega_s + \frac{\sin(2\omega_s)}{2}\right].$$

Finally, the S fraction from this model (and the corresponding correction factor f) are obtained as the ratio of Eq. (15) to Eq. (14). Note that the resulting expressions depend on k_t and are independent of the normalization constant L_z.

Although this simple model follows an overcast sky radiance model and has no explicit dependence on the Sun's position (other than treating separately the Sun's position in half-hemispheres), it has been compared to experimental data and found to be an improvement over Drummond's isotropic approximation. In particular, Muneer & Zhang (2001) report that the negative bias of the isotropic correction is reduced from -15.6 W/m^2 to -0.7 W/m^2 under clear-sky conditions ($k_t > 0.6$) while small positive biases are obtained for $k_t \leq 0.6$. Other evaluations show similar improvements over the isotropic model (López et al., 2004; Sánchez et al., 2012).

2.2.2. Vartiainen and Brunger (VB)

Brunger & Hooper (1993a) proposed an expression for the sky radiance that explicitly depends on the Sun's position,

$$L_p(\theta, \varphi) = G_d \left[\frac{a_0 + a_1 \cos\theta + a_2\, e^{-a_3 \psi}}{\pi\,(a_0 + 2a_1/3) + 2a_2\, I(\theta_z)} \right], \tag{16}$$

where $I(\theta_z)$ is such that the sky radiance L_p satisfies Eq. (3),

$$I(\theta_z) = \left[\frac{1 + e^{-a_3\pi/3}}{1 + a_3^2} \right] \cdot \left[\pi - \left(1 - \frac{2}{\pi a_3} \cdot \frac{1 - e^{-a_3 \pi}}{1 + e^{-a_3\pi/2}} \right) \times \left(2\theta_z \sin\theta_z - 0.02\,\pi\, \sin\left(2\theta_z\right) \right) \right]. \tag{17}$$

The first factor in Eq. (17) originally appeared with an erratum, corrected in Brunger & Hooper (1993b). The Sun's position dependence appears through ψ, the angle subtended between a given sky element (θ, φ) and the Sun's position (θ_z, φ_s).

The dependence on the sky conditions is introduced by considering the coefficients a_i as discrete functions of the clearness index k_t and the diffuse fraction, $f_d = G_d/G_h$. This last variable is not known a priory if the diffuse irradiance is measured with a shadow-band. In our implementation we used the isotropic correction factor to estimate f_d from the measured diffuse irradiance, G_{du}. No significant difference was observed when compared to using the reference value of G_d. The coefficients a_i in Eq. (16) are given in Brunger & Hooper (1993a) for a matrix of 9×9 bins in the (k_t, f_d) space. These coefficients were determined by adjusting the model (using non-linear regression) to one year of data from sky scans made in Toronto, Canada (latitude $\phi = 43.67°$). In Vartiainen (1999), this radiance distribution was used to calculate the diffuse irradiance intercepted by a shadow-band performing the numerical integration of Eq. (5). Monthly averaged correction factors were calculated using one year of data for Helsinki, Finland (latitude $\phi = 60°$), and were compared with Drummond's isotropic correction, the all-sky Perez et al. (1993) model (Subsection 2.2.3) and LeBaron et al. (1980) model (Subsection 2.3.3). For that location, Vartiainen found that the LeBaron et al. model produces slightly lower correction factors during summer.

2.2.3. Vartiainen and Perez (VP)

The sky luminance distribution from Perez et al. (1990), used in the all-sky Perez's model for diffuse solar irradiance (Perez et al., 1993), has also been used to calculate the S fraction and its corresponding correction factor (Vartiainen, 1999). In the context of sky illuminance, this model has been shown to outperform several other illuminance models (Perez et al., 1990). With the proper normalization, it can be interpreted as a sky radiance distribution (Gracia et al., 2011),

$$L_p(\theta, \varphi) = C\,(1 + a\,e^{b/\cos\theta}) \cdot (1 + c\,e^{d\psi} + e\cos^2\psi), \tag{18}$$

in terms of the angle ψ. The normalization constant C is determined in terms of G_d, using Eq. (3). Each of the coefficients $(a, b, \ldots e)$ can be related to different aspects of the radiance distribution and depend on the sky condition. As expected, this distribution peaks at the Sun's position ($\psi = 0$) so it captures the circumsolar contribution to diffuse irradiance.

The sky condition is originally modelled in Perez et al. (1990) by a set of two dimensionless parameters: the sky brightness (or diffuse clearness index), $k_d = G_d/G_{0h}$, and the modified sky clearness parameter, ϵ', defined as

$$\epsilon' = 1 + \frac{G_b/G_d}{1 + 1.041\,\theta_z^3}, \tag{19}$$

where θ_z is expressed in radians. When the sky condition is characterized in terms of k_t and f_d, these two parameters (k_d and ϵ') can be obtained as

$$k_d = k_t\,f_d \qquad \text{and} \qquad \epsilon' = 1 + \frac{1/f_d - 1}{\cos\theta_z\,(1 + 1.041\,\theta_z^3)}. \tag{20}$$

The dependence of the sky radiance distribution on the sky condition is given through the vector of coefficients $x = (a, b, c, d, e)$, which satisfy

$$x(\theta_z, k_d, \epsilon') = x_1(\epsilon') + x_2(\epsilon')\,\theta_z + [x_3(\epsilon') + x_4(\epsilon')\,\theta_z]\,k_d. \tag{21}$$

Each of these functions x are analytical in (θ_z, k_d) but are discrete in ϵ', through the x_i values. The sky clearness parameter is grouped in eight bins of increasing sky clearness with boundaries: [1, 1.065, 1.230, 1.500, 1.950, 2.800, 4.500, 6.200, ϵ'_{max}], and the coefficients x_i for each bin are tabulated in Perez et al. (1993). An exception in Eq. (21) occurs for $x = c, d$ in the first bin $\epsilon' \in [1, 1.065)$. For these cases the coefficients are

$$c(\theta_z, k_d, \epsilon') = e^{\{[c_1 + c_2\,\theta_z]k_d\}^{c_3}} - c_4, \tag{22}$$

$$d(\theta_z, k_d, \epsilon') = -e^{[d_1 + d_2\,\theta_z]k_d} + d_3 + d_4\,k_d. \tag{23}$$

The tabulated values $x_i(\epsilon')$ reported in Perez et al. (1993) were obtained from over 1600 sky scans at the Lawrence-Berkeley Laboratory in California between 1985-86. In the same way as in the previous model (VB), in our implementation we used the isotropic correction factor to estimate f_d from the measured diffuse irradiance, G_{du}.

2.2.4. Comparison of parametric distributions

In Fig. 2 the four analytical sky radiance distributions (VP, VB, MZ, ISO) are compared for four different sky conditions ranging from clear sky to full overcast. Sky radiances are normalized with the isotropic sky radiance $L_p^{iso} = G_d/\pi$, which therefore appears as a horizontal line. Each panel shows the sky direction along the Sun's meridian, i.e. $\varphi = \varphi_s$ for all θ. The Sun's altitude is fixed and corresponds to an air mass of 1.5 ($\theta_z = 48.2°$). Both VB and VP radiances peak at the Sun's position and these peaks represent the circumsolar contribution to diffuse horizontal irradiance. The VP model under clear skies also shows some horizon brightening. The MZ model shows dependence with the polar angle, increasing towards the horizon under clear skies and decreasing under overcast condition. Under cloudy skies all models approach the isotropic distribution (see Fig. 2d).

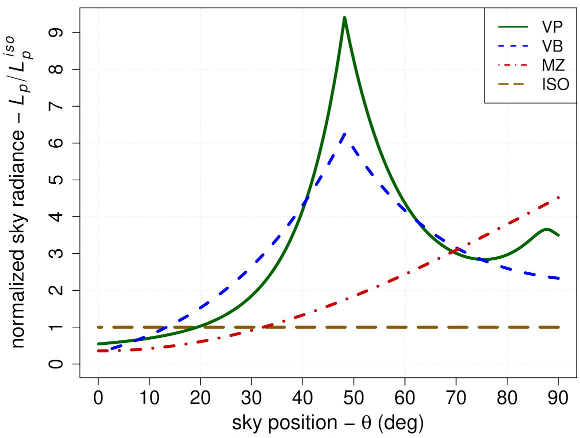

(a) Clear sky ($k_t = 0.80$, $f_d = 0.10$).

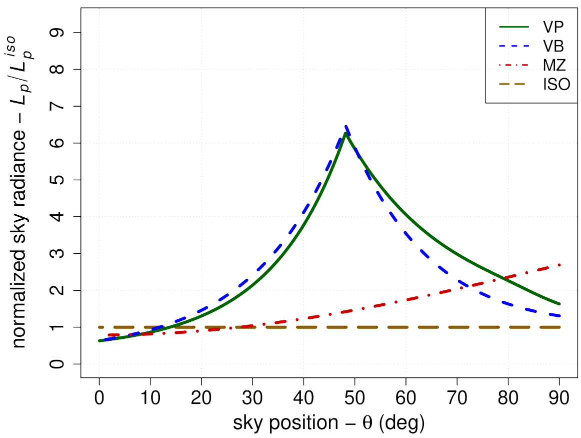

(b) Slightly cloudy ($k_t = 0.60$, $f_d = 0.40$).

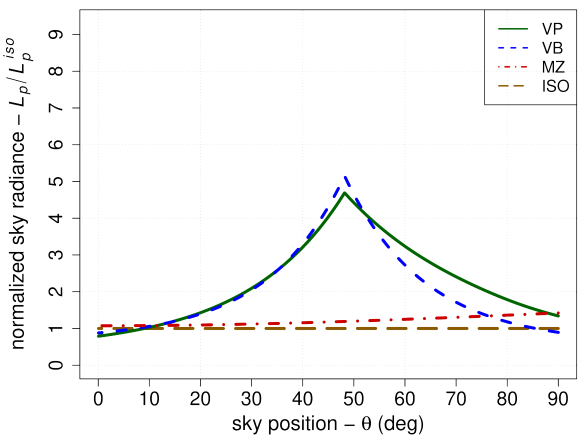

(c) Partly cloudy ($k_t = 0.40$, $f_d = 0.85$).

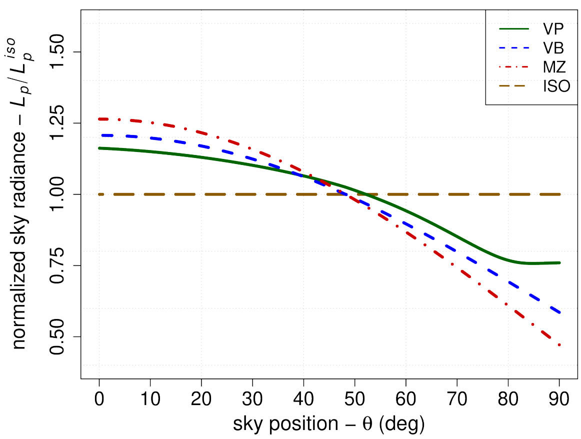

(d) Overcast ($k_t = 0.05$, $f_d = 1.00$).

Figure 2: Relative sky radiance (normalized by the isotropic radiance) for the three anisotropic models MZ, VB and VP for air mass 1.5 ($\theta_z = 48.2°$) along the Sun's meridian ($\varphi = \varphi_s$). Note that the y-axis has been modified for figure (d).

2.3. Phenomenological correction models

Working with sky radiance distributions is not straightforward, as it involves (except for the simplified MZ model) the numerical evaluation of double integrals and the use of LUT (look-up-tables) *for each data point*. Phenomenological models skip the sky radiance modeling and aim to obtain the correction factor directly. Five widely used phenomenological models are considered and a new proposal is described, optimized in this work for the region of interest.

2.3.1. Kasten et al. (KA)

In Kasten et al. (1983) the correction factor is parametrized as

$$f = A + B\left(\frac{k_{du}}{k_t}\right)^3 + C\,\delta + \frac{D}{\ln(1/\tau_{bu})}, \tag{24}$$

where $k_{du} = G_{du}/G_{0h}$ and $\tau_{bu} = G_{bu}/G_0$ are the diffuse clearness index and the beam transmittance of the uncorrected solar irradiance components, respectively. These dimensionless variables satisfy $\tau_{bu} = k_t - k_{du}$, so the beam transmittance is derived from k_t and k_{du}, restricted to $\tau_{bu} \geq 0$.

The constants of Eq. (24) were determined by Kasten et al. from less than one year of hourly data for Hamburg, Germany, using a plane shadow-band with $b/r = 0.169$. A pyranometer under a shade-disk device mounted on a solar tracker was used as the reference measurement and the reported values were $A = 1.161$, $B = -0.112$, $C = 0.0009$ and $D = -0.0246$.

2.3.2. Steven et al. (ST)

Steven (1984) proposed an all-sky method that takes into account the anisotropy due to the circumsolar region. The fraction of diffuse irradiance blocked by the shadow-band is expressed as $S = q\,S_0$, where S_0 corresponds to the isotropic case. The anisotropic correction q is parametrized as

$$q = 1 - C\,\xi + \frac{C}{I_1}, \tag{25}$$

where I_1 is given by Eq. (8), ξ is a constant related to the angular width of the circumsolar region ($\xi = 0.60$ rad is the value used in Steven (1984)), and C is related to the relevance of the anisotropic effects. It is expressed as a function of the relative sunshine hours for the day, $n_r = N/N_0$, as measured by a Campbell-Stokes heliograph,

$$C(n_r) = \frac{C_0\,n_r}{1 - \xi\,C_0\,(1 - n_r)}. \tag{26}$$

Anisotropic effects are less relevant for cloudy days ($n_r = 0$), and for a clear day ($n_r = 1$) this expression reduces to C_0, which is given as $C_0 = 1.01$ in Steven (1984). In sum, in order to allow for particular local climatic conditions, this model can be considered to depend on two adjustable constants (C_0 and ξ) and on the relative sunshine duration for the day, n_r.

2.3.3. LeBaron et al. (LB)

LeBaron et al. (1990) develop a Look Up Table (LUT) model for the correction factor f. Two years of hourly data from two sites in the U.S. (Albany, NY, and Bluefield, WV) were used to define the model in terms of four variables. One of them is the isotropic correction factor, $f_0 = 1/(1 - S_0)$, with S_0 from Eq. (7). The solar zenith angle, θ_z, is the second variable. The other two are the diffuse clearness index k_d and the sky clearness parameter without the solar zenith angle correction,

$$\epsilon = 1 + \frac{G_b}{G_d}. \tag{27}$$

The parameters k_d and ϵ are calculated using the uncorrected diffuse and beam irradiances, G_{du} and G_{bu}, which satisfy the closure relation, Eq. (1). Each parameter is binned in four categories with the boundaries shown in Table 1, resulting in a LUT with $4^4 = 256$ combinations. $f_{0,max}$ and ϵ_{max} are the maximum experimental values for these variables. The correction factors tabulated in LeBaron et al. (1990) vary between 0.935 and 1.248, with the values lower than unity indicating that some reflection from the inner part of the shadow-band was incident on the pyranometer.

index	variable / category		**1**	**2**	**3**	**4**
i	θ_z (^{o})	0	35	50	60	90
j	f_0	1.000	1.068	1.100	1.132	$f_{0,max}$
k	ϵ	1.000	1.253	2.134	5.980	ϵ_{max}
l	k_d	0.000	0.120	0.200	0.300	1.000

Table 1: Boundaries for the four categories of the LB model. The index column refers to the notation in LeBaron et al. (1990).

LeBaron et al. (1990) validate this model with independent data sets for both sites and show that it improves the isotropic correction factor, especially under partly clear skies when diffuse irradiance tends to be high and anisotropy effects are most important.

2.3.4. Batlles et al. (BA, BB)

Batlles et al. (1995) builds on LeBaron et al. model by considering the same four parameters and replacing the LUT with two alternative linear parametrizations for the correction factor.

The first proposal (named BA here) parametrizes f as

$$f = a\, f_0 + b\, \ln(k_d) + c\, \ln(\epsilon) + d\, e^{-1/\cos\theta_z}, \tag{28}$$

with a, b, c, d empirical constants fitted to the data. The authors note that the sky clearness parameter ϵ is one the most relevant predictors and propose a refined version (BB) with four categories in ϵ,

$$f = \begin{cases} a_1\, f_0 + b_1\, \ln(k_d) + d_1\, e^{-1/\cos\theta_z} & \epsilon \leq 3.5 \\ a_2\, f_0 + b_2\, \ln(k_d) + d_2\, e^{-1/\cos\theta_z} & 3.5 < \epsilon \leq 8 \\ a_3\, f_0 + b_3\, \ln(k_d) & 8 < \epsilon \leq 11 \\ a_4\, f_0 + b_4\, \ln(k_d) & \epsilon > 11. \end{cases} \tag{29}$$

Batlles et al. (1995) fit the coefficients in Eqs. (28) and (29) using three years of data for Madrid (hourly) and for Almeria (5-min) in Spain, based on Eppley shadow-bands with $b/r \approx 0.24$. A third of the data set was reserved for the validation of both models. As for the previous models, the parameters k_d and ϵ in BA and BB models are calculated using the uncorrected diffuse and beam irradiances, G_{du} and G_{bu}.

2.3.5. New proposal (NP)

After analyzing the performance of the BB method with different ϵ bin structures, a large variability between the first and last bins in Eq. (29) was observed. We consider a new linear model inspired in Eq. (28), with the addition of a constant (which reduces the mean bias) and with eight bins in ϵ', to allow a fit to each sky condition, similar to the VP model. The use of the modified sky clearness parameter in eight bins is found to improve performance (this parameter is also calculated using the uncorrected diffuse irradiance). The new proposal can be summarized as,

$$f = a_i\, f_0 + b_i\, \ln(k_d) + c_i\, \ln(\epsilon') + d_i\, e^{(-1/\cos\theta_z)} + e_i, \tag{30}$$

for ϵ' in the eight bins ($i = 1, \ldots 8$) as defined in Perez et al. (1993). Boundaries in ϵ' for these categories and the locally adjusted coefficients can be found in Table A.7.

3. Data and quality control

3.1. Data set description

A data set for a one year period (2019-2020) was generated at the Solar Energy Laboratory, located in a semi-rural environment at Salto, Uruguay (latitude $\phi = -31.27°$, longitude $\psi = -57.88°$, altitude $h = 59$ m above sea level). As mentioned in the introduction, the site is representative of a broad region in south-eastern South America, known as Pampa Húmeda, with a temperate climate designated Cfa in the updated Köppen-Geiger classification (Peel et al., 2007).

A Kipp & Zonen CM-121B shadow-band was used to measure the uncorrected diffuse irradiance, G_{du}. It has a U-shape profile with $b/r = 0.185$ (Kipp & Zonen , 2004). The reference global and diffuse horizontal measurements were obtained with two Kipp & Zonen CMP10 pyranometers (spectrally flat, Class A according to the ISO 9060:2018 standard). The pyranometer used to measure the reference diffuse irradiance was behind a standard shading-sphere assembly mounted on a SOLYS2 precision solar tracker. A Kipp & Zonen CHP1 pyrheliometer, mounted on the same tracker, was used to measure the DNI (used in this work for quality-check only). All these instruments were last calibrated in July 2018 according to the relevant ISO standard by the Solar Energy Laboratory (Abal et al., 2018) against a secondary standard (Kipp & Zonen CMP22) which provides traceability to the World Radiometric Reference.

Measurements were recorded at 1-minute time resolution between May 2019 and June 2020 and later integrated to 5-min intervals. This resulted in a 5-min data set with 57990 records of the reference variables (G_h, G_d, G_b) and 51881 records of the shadow-band variable G_{du}. The data set is restricted to diurnal records ($\cos\theta_z > 0$) and then processed for quality control using 10 filters, applied independently. The original data set includes a little bit more than one year data to compensate seasonal unbalances found after filtering. Each season is adequately represented in the final data set.

3.2. Quality control

Quality control is extremely important when trying to evaluate small effects from the data. The correction factors are not large (representing corrections under 15%) and the differences between them are much smaller, so a careful quality control procedure is required in order to remove potentially erroneous or atypical data records from the data set.

The set of quality-control procedures is based on the BSRN (Baseline Solar Radiation Network) recommended filters (McArthur, 2005) using local coefficients. These are supplemented with a few additional criteria, adopted after inspection of the data in the dimensionless (k_t, f_d) and (k_t, τ_b) spaces.

The quality filtering procedure is summarized in Table 2 and Fig. 3. Three BSRN filters (F1 to F3 in Table 2) apply an upper bound to the measured irradiances, G, as

$$G \leq G_0\, p\, (\cos\theta_z)^a + c, \tag{31}$$

where p, a and c are parameters which can be locally derived for each filter from F1 to F3 by inspection of each tested variable (G_h, G_d, G_b). Filter F4 sets a minimum solar altitude, $\alpha_s > 10^\circ$ or $\cos\theta_z > 0.174$, discarding low-altitude measurements which are affected by larger cosine errors. Filter F5 tests that the three reference irradiance components satisfy the closure relation of Eq. (1) with a tolerance of 8% of the G_h average, to allow for experimental error. This filter is only applied if $G_h > 50$ W/m^2, as indicated in the BSRN guidelines. Filter F6 tests for $f_d \leq 1.03$, allowing a 3% tolerance for experimental error in the reference diffuse fraction measurement. Filter F7 removes points of low k_t and low f_d, mostly associated with very low-irradiance measurements under heavy overcast conditions. Filter F8 is the upper bound $k_t < 1$, which excludes a few short-lived over irradiance events, rarely found in the 5-min records. Filter F9 tests for consistency between the uncorrected diffuse irradiance G_{du} and the reference value G_d: the experimental correction factor $f_e = G_d/G_{du}$ is required to be within $1 \leq f_e \leq 1.5\, f_0$ (internal reflections in the CM-121B shadow-band can be neglected). The lower limit proved to be useful to discard misaligned shadow-band data. The upper limit of $1.5\,f_0$ was determined by visual inspection of the f_e/f_0 histogram and only discards a few outliers. Finally, filter F10, inspired in the SERI-QC procedure (Maxwell et al., 1993), tests for anomalous clear-sky data, requiring $\tau_b < k_t - k_{d,min}$, with $k_{d,min} = 0.06$ determined from inspection of the (k_t, τ_b) diagram. Filters F2, F6 and F7 were applied also to the isotropically corrected diffuse horizontal measurement, G_{dc}, and are indicated in Table 2 as F2B, F6B and F7B, respectively. After the filtering procedure, about 1/3 of the data is discarded and a clean data set with 36939 5-min records satisfying all filters is obtained.

filter	condition	variables	input	output	% discarded
F1	Eq. (31)	G_h	56950	56926	0.04
F2	Eq. (31)	G_d	56918	56877	0.07
F2B	Eq. (31)	G_{dc}^{iso}	51881	50571	2.53
F3	Eq. (31)	G_b	54336	54336	0.00
F4	$\cos\theta_z > 0.174$	all	57990	49738	14.23
F5	Eq. (1)	G_h, G_d, G_b	54335	53097	2.28
F6	$f_d < 1.03$	G_h, G_d	56918	55472	2.54
F6B	$f_{dc}^{iso} < 1.03$	G_h, G_{dc}^{iso}	51881	43826	15.53
F7	$k_t < 0.20$ & $f_d > 0.80$	G_h, G_d	54336	54104	0.43
F7B	$k_t < 0.20$ & $f_{dc}^{iso} > 0.80$	G_h, G_d^{iso}	50890	50768	0.24
F8	$k_t < 1$	G_h	56950	56860	0.16
F9	$1 \leq f_e < 1.5\,f_0$	G_d, G_{dc}^{iso}	51880	45181	12.91
F10	$\tau_b < k_t - 0.06$	G_b, G_h	54336	54104	0.43
all		all	57990	36939	36.3

Table 2: Details of the filtering process applied on diurnal data records.

In addition, the ST model requires daily sunshine duration data (defined by the WMO as the period of time in a day during which $G_b > 120$ W/m^2). This variable is highly correlated with the average daily global solar irradiation. We use a series of sunshine duration measured by a Campbell-Stokes heliograph recorded at the National Agronomic Research Institute (INIA) site at Salto Grande, located 3 km away from the site of our irradiance measurements.

4. Methodology

4.1. Model implementation and local adaptation

The nine pre-existing correction models described in Section 2 were implemented and tested, both in their original and locally adapted versions. The assessment of the original versions, i.e. using the published

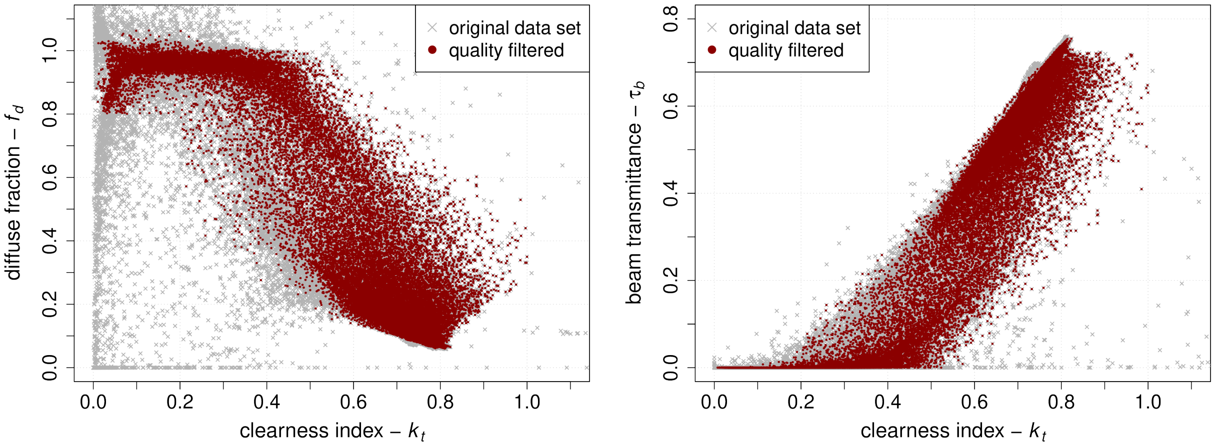

(a) f_d vs k_t diagram.

(b) τ_b vs k_t diagram.

Figure 3: Results of the data quality control procedure represented in two dimensionless spaces (Maxwell et al., 1993). The original data is plotted as gray crosses and the quality filtered data as red circles.

coefficients of the original models, allows to evaluate the baseline uncertainties in the target region when used as a generic (or universal) correction model. The local adaptation of these methods enhances their performance and provides either new local coefficients or locally adjusted correction factors. It also provides an adequate comparison context for the novel proposal of this work, which is obviously only tested with local adaptation.

4.1.1. Original models' implementation

The sky radiance models VB and VP are implemented via numerical integration of Eqs. (3) and (5) using the corresponding sky radiance function. In the case of the MZ model, the sky radiance L_p is implemented analytically (Subsection 2.2.1). For the phenomenological models KA, BA and BB, the Kasten's formula (Eq. (11)) was used to transfer the correction factors to the particular model band geometry to the CM-121B shadow-band used in this work. For the LB model this transfer could not be applied because the geometry of the LB shadow-band was not provided in LeBaron et al. (1990). The ST model is applicable to different shadow-band geometries by simply using the correct θ_0 value in the isotropic fraction S_0, Eq. (7). Drummond's isotropic correction function (DR) is also tested and it provides a baseline for the corrections.

4.1.2. Local adaptation

For local adaptation, models are separated into two categories as follows:

i) Those whose coefficients can be locally adjusted by using the shadow-band and reference diffuse measurements (KA, ST, LB, BA, BB and NP).

ii) Those whose coefficients can not be locally adjusted, either because the diffuse irradiance information is not enough to perform the adjustment, or because the model has too many or no parameters to tune (DR, MZ, VB and VP).

The phenomenological models discussed in Subsection 2.3 belong to type (i). On the other hand, the VB and VP sky-radiance distributions have $4 \times 48 = 192$ and $8 \times 20 = 160$ adjustable coefficients, respectively, and a proper adjustment of these parameters requires directional sky radiance measurements from an sky scanner. Due to this the sky-radiance models (including also the MZ model) belong to type (ii). The DR model is included in this second category as it has no adjustable parameters.

The locally-adjusted versions of type (i) models are obtained from local data using a standard random-sampling and cross-validation procedure. Depending on the model, linear or non-linear multiple regression is used. For type (ii) models, a site-adaptation post-procedure is required. A simple linear site-adaptation function (Polo et al., 2016) is used, so that the corrected diffuse irradiance is

$$G_{dc} = a\,(f\,G_{du}) + b, \tag{32}$$

where a and b are the slope and intercept of the linear fit, respectively, found by standard linear regression. This site-adaptation allows for a fair comparison between all locally-adjusted models. Both the site-adaptation and the local fits were performed by random sampling and cross-validation, using 60% of the data for local adaptation and 40% for validation. The 60/40 random split was repeated 100 times and the average coefficients and performance indicators are calculated for the ensemble.

The original and locally fitted coefficients for the phenomenological models are provided in the Appendix in Tables A.6 and A.7, and the values of a and b for the site-adapted models are listed in Table 3 below. The intercept (b) is small for all models and the slope correction (a) varies from $\simeq +9\%$ (MZ) to $\simeq -5\%$ (VB). The slope correction for the DR model is consistent with the known 3-4% underestimation from the isotropic approximation.

coef.	**DR**	**MZ**	**VB**	**VP**
a (no unit)	1.0310	1.0908	0.9502	0.9569
b (W/m^2)	1.0300	-3.0251	-1.4992	0.1031

Table 3: Coefficients for the site-adaptation of analytical models, Eq. (32).

4.2. Performance metrics

The performance assessment is done by using three common metrics, namely, the Mean Bias Deviation (MBD), the Root Mean Square Deviation (RMSD) and the Kolmogorov-Smirnov Integral (KSI) (Gueymard, 2014). These quantities are defined as follow,

$$\mathrm{MBD} = \frac{1}{n}\sum_{i=1}^{n}(\hat{y}_i - y_i), \qquad \mathrm{RMSD} = \left[\frac{1}{n}\sum_{i=1}^{n}(\hat{y}_i - y_i)^2\right]^{\frac{1}{2}}, \qquad \mathrm{KSI} = \int_0^{y_m} |F(y) - \hat{F}(y)|\, dy, \tag{33}$$

where y_i stands for the reference value (G_d), $\hat{y}_i$ for the corrected value (G_{dc}), y_m for the maximum in $\{G_d, G_{dc}\}$ and F and $\hat{F}$ are cumulative distributions functions of y_i and $\hat{y}_i$, respectively. This set of indicators has been used successfully in this region to assess the performance of empirical diffuse fraction models (Abal et al., 2017) and satellite based solar assessment models (Laguarda et al., 2020). These metrics have units of $\mathrm{W/m^2}$ but can be expressed in relative terms (rMBD, rRMSD and rKSI) as a percentage of the average reference value, $\bar{G}_d$. Since each of them quantifies a different similarity aspect between the measured and corrected data sets, it is convenient to define a collective performance indicator as,

$$\mathrm{CPI} = \frac{1}{3}\left(|\mathrm{rMBD}| + \mathrm{rRMSD} + \mathrm{rKSI}\right). \tag{34}$$

This global index, which is expressed as a percentage of the average reference value, $\bar{G}_d$, is used as an indicator for overall model performance.

5. Results and discussion

In this section the correction models' performances are discussed, both in their original and locally adapted versions. The coefficients for both versions of each model are provided in Tables A.6 and A.7.

5.1. Original models

The performance results for the nine models with their original coefficients are presented in Table 4. The metrics of Subsection 4.2 were calculated for the all-sky data set and also for three subsets (I, II, III) associated to different sky conditions according to k_t: clear sky, partly cloudy skies and overcast skies. Fig. 4 shows the corresponding nine scatter-plots between the reference diffuse measurement and the shadow-band corrected diffuse measurement, showing in color (online version) the k_t discrimination.

The lowest overall biases are observed for DR (underestimation) and ST model (overestimation). Around half of the models (including DR, which has a well-known negative bias) underestimate the diffuse irradiance. The underestimation of these models is present under the three sky conditions, with the exception of the DR model, which changes its behavior to overestimation under overcast sky. MZ is the only sky radiance-based model that underestimates diffuse irradiance. Most models have biases within ±6%, except for the BA and BB phenomenological models, which show high underestimation biases when used with their original coefficients. For these two models, large underestimation occurs under the three sky conditions, being worst under overcast sky for the BB model and under clear sky for the BA model. This behavior can also be

sky condition	metric (%)	DR	MZ	VB	VP	KA	ST	LB	BA	BB
all sky	rMBD	-2.3	-6.4	6.3	4.4	6.2	1.6	6.3	-21.1	-21.8
	rRMSD	7.3	11.0	10.2	8.4	9.0	6.3	9.6	25.2	28.3
	rKSI	2.5	6.4	6.3	4.4	6.2	1.7	6.3	21.0	21.9
$\bar{G}_d = 143.7$ W/m^2	CPI	**4.0**	7.9	7.6	5.8	7.2	**3.2**	7.4	22.4	24.0
mostly clear sky	rMBD	-2.5	-5.9	6.5	5.0	10.9	2.4	5.6	-19.7	-34.8
($k_t \geq 0.6$)	rRMSD	8.2	11.5	9.3	8.8	13.2	7.2	8.8	22.3	41.0
data count: 22950	rKSI	2.8	5.9	6.5	5.1	10.9	3.0	5.6	19.7	34.8
$\bar{G}_d = 115.7$ W/m^2	CPI	**4.5**	7.7	7.4	6.3	11.7	**4.2**	6.7	20.6	36.9
partly cloudy	rMBD	-2.7	-7.4	5.8	3.5	1.4	0.5	6.6	-17.7	-8.1
($0.2 < k_t < 0.6$)	rRMSD	6.1	9.9	9.5	7.2	3.9	5.0	9.1	20.6	12.9
data count: 10695	rKSI	2.7	7.4	5.8	3.9	1.4	0.7	6.6	17.7	8.3
$\bar{G}_d = 221.2$ W/m^2	CPI	3.8	8.2	7.1	4.9	**2.3**	**2.1**	7.4	18.7	9.8
overcast	rMBD	2.4	-3.1	9.1	6.1	2.8	3.6	9.9	-61.5	-15.0
($k_t \leq 0.2$)	rRMSD	4.3	5.0	13.9	9.2	4.1	5.5	11.3	65.7	16.0
data count: 3285	rKSI	2.4	3.0	9.1	6.1	2.8	3.6	9.9	59.9	15.0
$\bar{G}_d = 87.5$ W/m^2	CPI	**3.1**	3.7	10.7	7.1	**3.2**	4.2	10.4	62.4	15.3

Table 4: Performance indicators for the nine original models, expressed as a percentage of the average reference diffuse irradiance ($\bar{G}_d$). The best performing models in terms of the combined index (CPI) are highlighted in boldface.

observed in the scatter-plots of Fig. 4, panels (g) and (h), especially the large overcast underestimation of the BA model. Most models have an overall rRMSD between 6 and 11%, with the exception of the BA and BB models affected by the large bias deviations already discussed. The lowest rRMSD are observed, again, for the ST and DR models. The rKSI metric orders the models in the same way as the rRMSD, but enhances the differences within values. As a result, the overall CPI metric discriminates the original models roughly into three groups:

(a) The best performing original models (ST and DR).

(b) Middle-range models (VP, KA, LB, VB and MZ) that may be used in the region in its original version but with higher uncertainties than the simple DR model.

(c) Models that should not be used in region without local adjustment (BA and BB).

The sky condition discrimination shows further insights. As shown in the data counts of Table 4, the overall metrics are dominated by the mostly clear sky condition, the prevailing situation in the local climate. The best performing model under clear skies is, consistently, the ST model, followed by the DR model. However, under the highly anisotropic partly cloudy conditions, the first and second models are ST

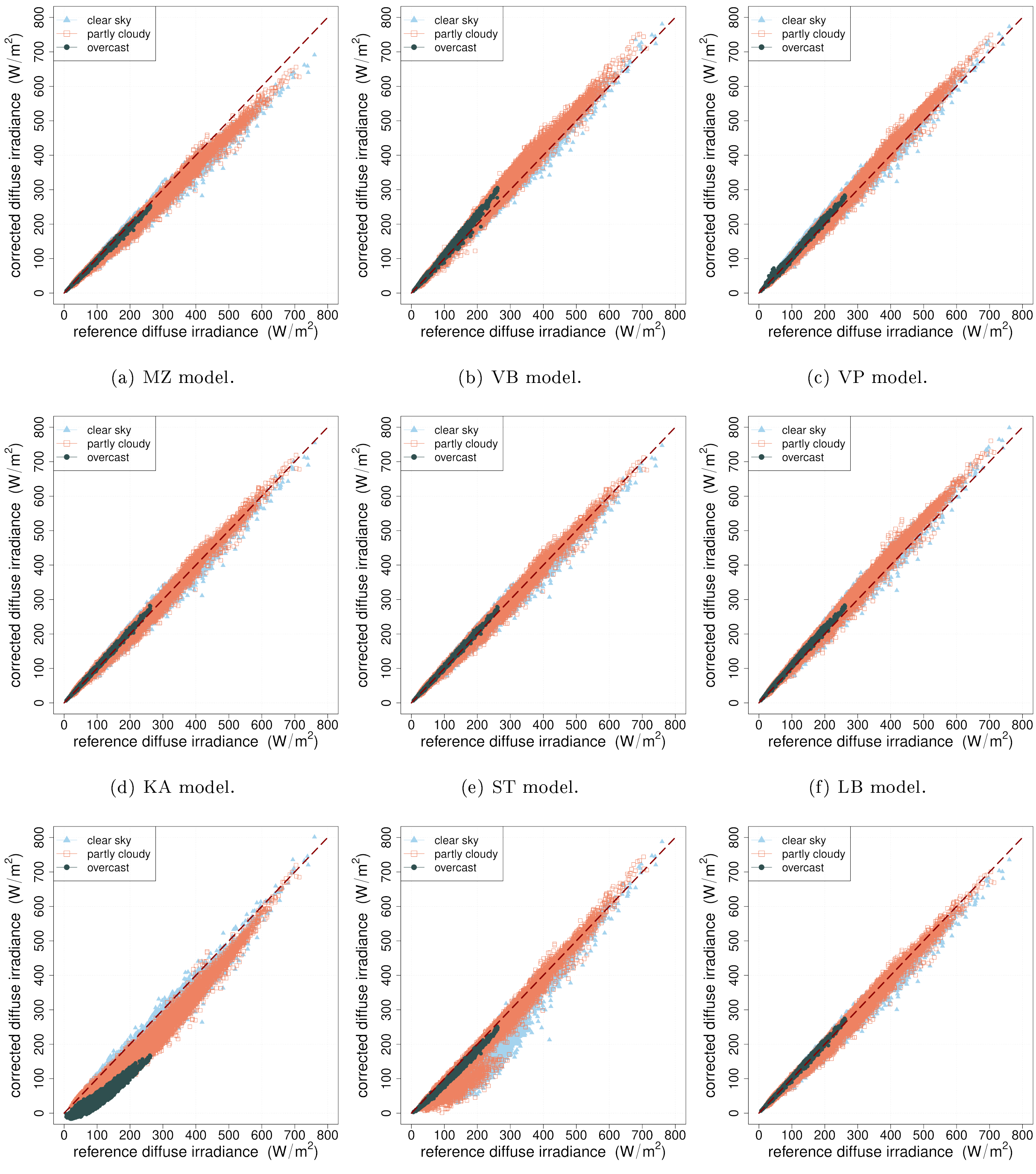

(a) MZ model.

(b) VB model.

(c) VP model.

(d) KA model.

(e) ST model.

(f) LB model.

(g) BA model.

(h) BB model.

(i) Isotropic model (DR).

Figure 4: Scatter-plots between the reference diffuse measurement (G_d) and the corrected shadow-band diffuse measurement (G_{dc}) for the nine pre-existing models with their original coefficients or non site-adapted (color in online version).

and KA, respectively. Furthermore, the KA model is also the second option for overcast condition, very close to the DR model. Of course, the DR model is the best model under overcast conditions, where the isotropic assumption holds better (see Fig. 2 panel (d)). The KA model is indeed a good choice for partly cloudy and overcast conditions and deserves further investigation in other regions. Its overall all-sky performance is not within the best ones because of its poor performance under clear sky, with a high overestimation bias of $\simeq 11\%$. An interestig alternative (not explored in this first article on the subject) is to use a combination of these models for different sky conditions. For instance, for this region, the ST model can be used for mostly clear and partly cloudy skies and the DR model for overcast conditions ($k_t \leq 0.2$). Without local adaptation and in the absence of sunshine hours records, i.e. when only the uncorrected shadow-band measurement is available, the best combination for this region is to use the DR model for clear sky and overcast conditions and the KA model for partly cloudy.

In sum, the ST model is the best generic model to use in the Pampa Húmeda region without local adaptation and it is the only one to outperform the isotropic method. However, it requires daily sunshine duration records and, in the absence of such information, the simple Drummond correction is the best choice, at least for this target region. This claim may be also applicable for other regions and climates, and also the overall performance may be improved by using a models' combination, but all these require specific studies.

5.2. Locally adapted models

The details on the local adaptation of all models have been presented in Subsection 4.1.2. The results for the locally adapted models are presented in Table 5, with the same metrics and sky condition discrimination as the previous analysis for original models. However, in this case, the performance indicators are calculated via the random sampling and cross-validation procedure. The locally adjusted versions perform better and their metrics become closer, with KSI gaining in importance (it can resolve small differences between similar performing models). Overall biases are within $\pm 1\%$, being negligible in most cases, with the exceptions of the ST, KA and LB models. In the rRMSD metric two groups of models are distinguishable, those around 4-5% (KA and NP) and the rest with 6-7%. In this case, the rKSI order (measuring the similarity between cumulative distributions) does not mimic the rRMSD, providing another models' order without distinguishable groups. The scatter-plots of locally adapted models are quite similar, so in this section we will only show the most relevant ones. The full set of scatter-plots are provided in high resolution in the online version of this article.

The new model proposed in this work (NP), inspired in the BA and BB models, is the best performing local model for the target region. It is unbiased and has the lowest overall rRMSD and rKSI, and presents the best overall CPI with a small gap from the other models. These observations holds not only for all-sky conditions, but also for the three sky subsets. Fig. 5 shows the scatter-plot for this model in comparison with the baseline isotropic model. For the NP model, samples for the three sky conditions are centered

sky condition	metric (%)	DR	MZ	VB	VP	KA	ST	LB	BA	BB	NP
	rMBD	0.0	0.0	0.0	0.0	-0.7	0.8	-0.9	-0.1	0.0	0.0
all sky	rRMSD	6.5	6.2	6.9	6.2	4.9	6.2	6.9	6.2	6.3	4.7
	rKSI	0.9	0.6	0.7	1.4	1.2	1.2	1.8	0.8	0.7	0.4
$\bar{G}_d = 143.7\ \mathrm{Wm}^{-2}$	CPI	2.5	2.3	2.5	2.5	2.3	2.8	2.6	2.4	2.3	**1.7**
mostly clear sky	rMBD	-0.4	0.1	-0.1	0.6	-0.5	1.3	-1.2	-0.5	-0.3	0.0
($k_t \geq 0.6$)	rRMSD	6.9	6.7	6.9	7.1	5.9	6.9	7.5	6.6	6.7	5.8
data count: 22950	rKSI	1.7	1.3	1.7	1.9	1.3	2.6	2.7	1.4	1.2	0.6
$\bar{G}_d = 115.7\ \mathrm{Wm}^{-2}$	CPI	3.0	2.7	2.9	3.2	2.6	3.6	3.8	2.8	2.8	**2.1**
partly cloudy	rMBD	-0.1	-0.3	-0.1	-0.9	-1.0	0.0	-1.2	0.1	0.1	0.1
($0.2 < k_t < 0.6$)	rRMSD	5.6	5.3	6.2	5.0	3.8	5.0	5.8	5.4	5.5	3.5
data count: 10695	rKSI	1.1	1.0	1.4	1.6	1.2	0.7	1.2	1.1	0.9	0.5
$\bar{G}_d = 221.2\ \mathrm{Wm}^{-2}$	CPI	2.3	2.2	2.6	2.5	2.0	1.9	2.7	2.2	2.2	**1.3**
overcast	rMBD	4.4	2.3	2.0	1.7	0.9	3.5	4.6	0.9	1.8	-0.3
($k_t \leq 0.2$)	rRMSD	6.6	5.2	8.3	5.7	2.6	5.3	6.4	3.8	4.3	2.8
data count: 3285	rKSI	4.4	2.9	3.2	2.0	1.0	3.5	4.6	1.5	1.9	0.7
$\bar{G}_d = 87.5\ \mathrm{Wm}^{-2}$	CPI	5.1	3.4	4.5	3.1	1.5	4.1	5.2	2.0	2.6	**1.3**

Table 5: Performance indicators for the ten localized models, expressed as a percentage of the average reference diffuse irradiance ($\bar{G}_d$). The overall mean bias is under $\pm 1\%$ in all cases. The best performing models in terms of the combined index (CPI) are highlighted in boldface.

on the $x = y$ line (dashed-line in red), being essentially unbiased as the corresponding rMBD indicators also show in Table 5. The site-adapted isotropic model, as seen in Fig. 5, shows an overcast overestimation which is partially compensated by a clear sky underestimation. This also happens to several other models in Table 5, i.e. the LB model, to mention the weakest in this sense. The NP model also shows a smaller dispersion of the samples around the $x = y$ line for each sky condition. In fact, it is the lowest dispersion from all models, as shown by the rRMSD metrics in Table 5.

The NP model is an enhancement of the BB and BA models, which are the models that are most impacted by the local adaptation procedure. Comparison of Tables 4 and 5 shows that their performance metrics improve significantly, both under all-sky and discriminated by sky conditions. The scatter-plot of their local versions, Fig. 6, can be easily contrasted with the high deviations observed in the original versions, Fig. 4 panels (g) and (h). However, the NP model improves upon them (both in alignment and dispersion, or rMBD and rRMSD). The radical change in performance due to the local adaptation of these two models is also expected for the NP proposal, so this correction model should not be used in other regions or climates without local adaptation procedure. This also applies for the BB and BA models, as shown.

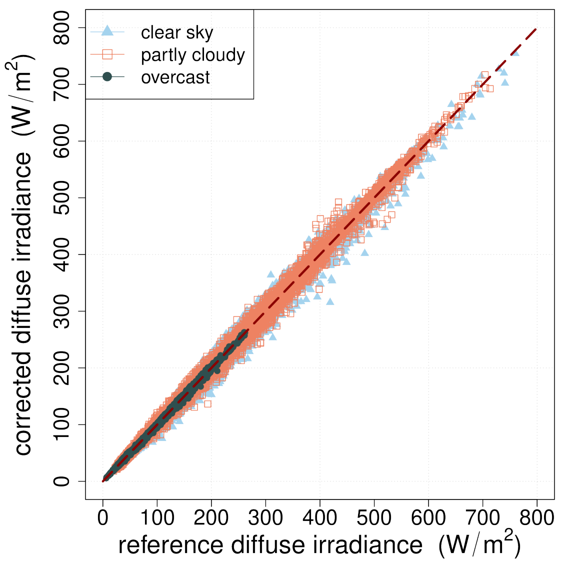

(a) Novel proposal (NP).

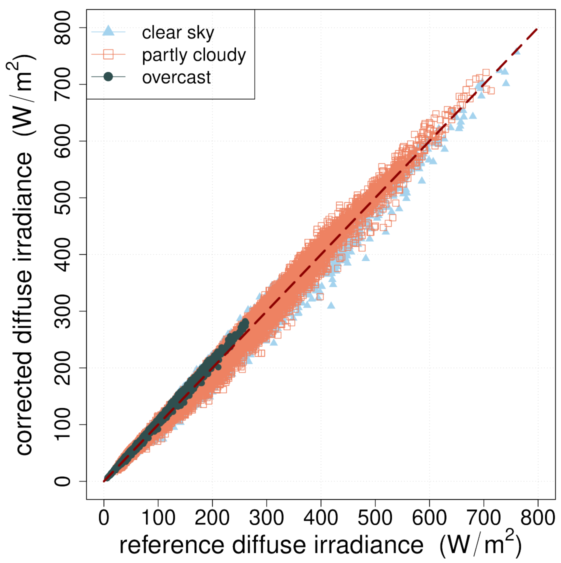

(b) Isotropic model (DR).

Figure 5: Scatter-plots between the reference diffuse measurement (G_d) and the corrected shadow-band diffuse measurement (G_{dc}) for the novel model of this work and the baseline isotropic model.

The evaluation of the NP model in other climates is required to test if the enhancements presented in this work imply also a modification of the model's robustness under different climates. In this sense, we provide in http://les.edu.uy/RDpub/JMRM_SBCF_model.zip a matlab program that runs, adjusts and evaluates the novel model based on a local set of data.

When locally adapted, several models are a good choice to use in the region. The second best performing model is the KA model, which presents low dispersion under each sky condition and low overall bias. This model is ranked in the top three positions of CPI both for all-sky and discriminated sky conditions and it has the best rRSMD under overcast sky, narrowly outperforming the NP model for this specific sky condition. Furthermore, the KA model has a good balance between accuracy and simplicity, as it only has 4 adjustable coefficients. By looking at the overall CPI, the BB, BA and MZ models achieve a similar ranking of 2.3-2.4%. The sophisticated VP and VB sky radiance models achieve similar performance than the rest. The unbiased isotropic model (site-adapted DR) is a simple alternative which, once locally adapted, yields similar results as more complicated models and can be considered as a good alternative. Since all localized models perform reasonably well, the selection of the correction model can be based on convenience and on the available information. The ST model, identified as the best generic model to use in the region, does not improve its performance metrics significantly when locally adapted. Its bias is reduced, but the rRMSD and rKSI is only slightly reduced, thus the model results in the worst ranked local version in spite of having the addition sunshine hours information. Consistently, the coefficients of this model do not vary too much between the

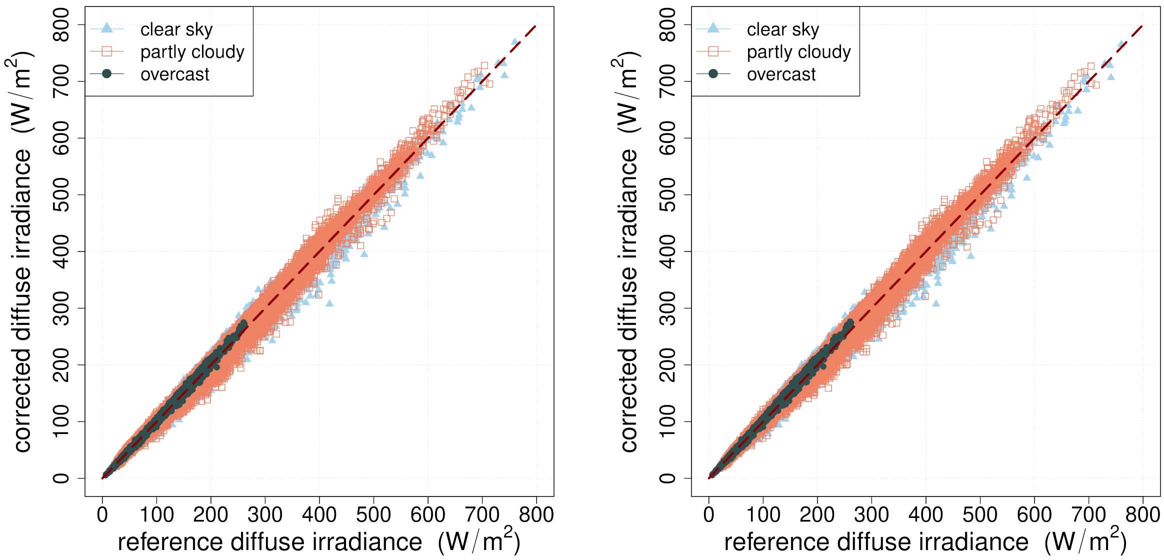

(a) BA model.

(b) BB model.

Figure 6: Scatter-plots between the reference diffuse measurement (G_d) and the corrected shadow-band diffuse measurement (G_{dc}) for the phenomenological models that where most improved by the local adaptation.

original and local versions (see Table A.6).

6. Conclusions

Phenomenological models used in solar resource assessment have different performance under different climates and the necessity and impact of local adaptation is often overlooked in the literature. In this work, an assessment of several shadow-band correction models for diffuse irradiance measurement in the Pampa Húmeda region is reported, both in their original and locally adapted forms, showing the impact of local adaptation on this kind of models. The evaluation includes a novel proposal which outperforms the pre-existing models for this region, even when they are locally adapted.

The best generic (i.e. without local adaptation) model for the Pampa Húmeda is the ST model (Steven, 1984), requiring additional daily sunshine duration information. If only shadow-band measurements are available, the best generic model for the region is the isotropic correction of Drummond (1956) (DR). This implies that the use of more sophisticated correction models without local adaptation, i.e. outside of the region for which they were derived, should be avoided, with the mentioned exception of the ST model. The DR model is known to underestimate diffuse irradiance by a small amount (confirmed by the results from this article) composed by an overestimation under cloudy skies and an underestimation under clear and partially cloudy conditions. A critical dependence of two models from Batlles et al. (1995) (labelled here as BA and BB) with the local adaptation was found, implying that they should not be used in this region without a previous local adjustment of their coefficients.

Rather than using generic models, it is preferable to use locally adapted versions. However, the work involved in local adaptation varies considerably between models. In this article we calculated the local coefficients and post-processing constants to use in the region for the ten models (including the novel proposal) analyzed, in order to reduce biases and enhance overall performance. Among locally adapted models, the performance differences are quite small and any of them may be used, hence the choice may be based on the user convenience for implementing the model and performing the local adaptation. The best performing model is the novel proposal made here, NP, with negligible bias and a rRMSD under 5%. It has the best performance metrics under all-sky conditions and under discriminated sky conditions (clear, partially cloudy, cloudy). As the model is an enhancement of the pre-existing BB and BA phenomenological models (Batlles et al., 1995), its performance is expected to be strongly dependent on local adaptation and its utilization is not recommended in other climates without the local adjustment, pending further studies to test its robustness under different climates. The local implementation of the NP model has the best performance but it requires to adjust 40 coefficients to local data. With simplicity in consideration, the locally adjusted KA (Kasten et al., 1983) model can be singled out, as it provides an overall low bias and low dispersion under each sky condition and has only four adjustable coefficients. In particular, it was found that the sophisticated sky radiance models do not provide any outstanding feature, nor in overall or sky-discriminated performance, nor in their generic or locally adapted versions, so their utilization is not found to report significant advantages over phenomenological models.

Acknowledgments

The authors acknowledge financial support from Comisión Sectorial de Investigación Científica (CSIC-Grupos), Universidad de la República (Udelar), Uruguay.

Appendix A. Models' coefficients

The values of the local coefficients for the phenomenological models (KA, ST, LE, BA, BB, NP) described in Subsection 2.3 are listed in the tables below. These are included here in order to make the localized versions of the models usable in the broad region (Pampa Húmeda) or in other regions with a similar climate (Cfa). The original coefficients are also reported (except the LB model), for completeness.

model					Reference
KA	A	B	C	D	Eq. (24)
original	1.161	-0.112	0.0009	-0.025	Kasten et al. (1983)
local	1.235	-0.191	-0.0362	-0.049	this work
ST	C_0	ξ (rad)			Eq. (25)
original	1.01	0.60			Steven (1984)
local	1.03	0.74			this work
BA	a	b	c	d	Eq. (28)
original	1.245	0.522	0.230	0.322	Batlles et al. (1995)
local	1.085	0.048	0.017	-0.047	this work

Table A.6: Coefficients for original and local versions of models KA, ST, BA.

model									Reference
BB	bin	ϵ_1	ϵ_2	a	b		d		Eq. (29)
original	1	1.0	3.5	1.178	0.207	-	0.122		Batlles et al. (1995)
	2	3.5	8.0	1.454	0.655	-	0.476		
	3	8.0	11.0	1.486	0.495	-	0		
	4	11.0	ϵ_{max}	1.384	0.363	-	0		
local	1	1.0	3.5	1.080	0.040	-	-0.043		this work
	2	3.5	8.0	1.007	-0.053	-	0.195		
	3	8.0	11.0	1.024	0.001	-	0		
	4	11.0	ϵ_{max}	1.033	0.013	-	0		
NP	bin	ϵ'_1	ϵ'_2	a	b	c	d	e	Eq. (30)
local	1	1.00	1.065	0.3775	-0.0087	0.6181	0.0919	0.5725	this work
	2	1.065	1.230	0.4151	0.0159	0.4852	-0.0202	0.6007	
	3	1.230	1.500	0.3818	0.0313	0.2051	-0.0477	0.7177	
	4	1.500	1.950	0.0645	-0.0478	0.0625	0.0676	1.0058	
	5	1.950	2.800	-0.1446	-0.1167	-0.0889	0.1531	1.2349	
	6	2.800	4.500	-0.2518	-0.1818	-0.1971	0.2529	1.3465	
	7	4.500	6.200	-0.2305	-0.2245	-0.2643	0.2304	1.3431	
	8	6.200	ϵ'_{max}	0.3101	0.1267	0.0705	-0.0714	0.9491	

Table A.7: Coefficients (original and local) for models BB, NP. The bins for BB are defined by $\epsilon_1 \leq \epsilon < \epsilon_2$. The bins for NP follow the same pattern but in ϵ' (rigth-open intervals) and are adapted from Perez et al. (1993).

$(i,j,1,1)$				$(i,j,1,3)$			
$\underline{1.051}$	$\underline{1.082}$	1.1298	1.1288	$\underline{1.051}$	$\underline{1.082}$	1.1286	1.1285
$\underline{1.051}$	1.1279	1.1294	1.1283	$\underline{1.051}$	1.1276	1.129	1.1292
1.1287	1.1273	1.1273	1.1301	1.1294	1.1279	1.1296	1.1321
1.1279	1.1286	1.1258	1.1353	1.1289	1.1294	1.1296	$\underline{1.156}$
$(i,j,2,1)$				$(i,j,2,3)$			
$\underline{1.051}$	$\underline{1.082}$	1.1282	1.1291	$\underline{1.051}$	$\underline{1.082}$	1.1278	1.1287
$\underline{1.051}$	1.1274	1.1293	1.1283	$\underline{1.051}$	1.1276	1.1278	1.1282
1.1292	1.1293	1.1279	1.1321	1.1288	1.1273	1.1282	1.1283
1.1287	1.1287	1.1297	1.1294	1.1289	1.1295	1.1288	1.1286
$(i,j,3,1)$				$(i,j,3,3)$			
$\underline{1.051}$	$\underline{1.082}$	1.1272	1.1297	$\underline{1.051}$	$\underline{1.082}$	1.1279	1.1287
$\underline{1.051}$	$\underline{1.082}$	1.1286	$\underline{1.156}$	$\underline{1.051}$	1.13	1.1289	1.1274
1.0944	$\underline{1.082}$	1.1217	1.133	1.1289	1.1274	1.1292	1.1283
1.1298	1.1261	1.1263	1.128	1.1291	1.129	1.1298	1.1284
$(i,j,4,1)$				$(i,j,4,3)$			
$\underline{1.051}$	$\underline{1.082}$	1.129	1.1287	$\underline{1.051}$	$\underline{1.082}$	$\underline{1.117}$	$\underline{1.156}$
1.1299	1.1286	1.129	1.1289	$\underline{1.051}$	$\underline{1.082}$	$\underline{1.117}$	$\underline{1.156}$
1.1287	1.1291	1.1291	1.1292	1.1261	1.1168	1.1328	1.1305
1.1288	1.1287	1.1284	1.1289	1.1293	1.1271	1.1319	1.1281
$(i,j,1,2)$				$(i,j,1,4)$			
$\underline{1.051}$	$\underline{1.082}$	1.1298	1.1282	$\underline{1.051}$	$\underline{1.082}$	1.1296	1.1293
$\underline{1.051}$	1.1296	1.1293	1.13	$\underline{1.051}$	1.1298	1.1284	1.1273
1.1282	1.13	1.128	1.1301	1.1283	1.1254	1.131	$\underline{1.156}$
1.1284	1.1289	1.1279	1.1329	1.1312	$\underline{1.082}$	$\underline{1.117}$	$\underline{1.156}$
$(i,j,2,2)$				$(i,j,2,4)$			
$\underline{1.051}$	$\underline{1.082}$	1.1339	1.1286	$\underline{1.051}$	$\underline{1.082}$	1.1299	1.1286
$\underline{1.051}$	1.1279	1.1296	1.1293	1.1271	1.1294	1.1297	1.1293
1.1229	1.132	1.1293	1.1286	1.1294	1.1288	1.1274	1.1295
1.1289	1.1274	1.1284	1.1301	1.1287	1.1282	1.1279	1.1285
$(i,j,3,2)$				$(i,j,3,4)$			
$\underline{1.051}$	$\underline{1.082}$	1.1293	1.1286	$\underline{1.051}$	$\underline{1.082}$	1.1258	1.1277
$\underline{1.051}$	1.1284	1.1287	1.1281	$\underline{1.051}$	1.1277	1.1278	1.1279
1.1282	1.1292	1.1307	1.1297	1.1279	1.1277	1.1292	1.1305
1.1304	1.1295	1.1283	1.1291	1.1282	1.1267	1.1277	1.1299
$(i,j,4,2)$				$(i,j,4,4)$			
$\underline{1.051}$	$\underline{1.082}$	1.1286	1.1289	$\underline{1.051}$	$\underline{1.082}$	$\underline{1.117}$	$\underline{1.156}$
1.1275	1.1282	1.1293	1.1298	$\underline{1.051}$	$\underline{1.082}$	$\underline{1.117}$	$\underline{1.156}$
1.1288	1.1288	1.1283	1.1287	$\underline{1.051}$	$\underline{1.082}$	$\underline{1.117}$	$\underline{1.156}$
1.1289	1.1289	1.129	1.1288	1.1283	1.1065	1.1307	1.1294

Table A.8: LUT with the 256 correction factors for the local LB model, described in Subsection 2.3.3. The bins (i, j, k, l) are defined in Table 1. In each sub-matrix, $i \rightarrow$ columns (1 to 4), $j \rightarrow$ rows (1 to 4). The header of each sub-matrix shows the values of $k \rightarrow \epsilon$ and $l \rightarrow k_d$. The underlined values correspond to empty category that are filled with the mean isotropic correction factor. The corresponding values for the original model can be found, in the same format, in LeBaron et al. (1990).

References

Abal, G., Aicardi, D., Alonso-Suárez, R., & Laguarda, A. (2017). Performance of empirical models for diffuse fraction in uruguay. *Solar Energy*, *141*, 166 – 181. doi:https://doi.org/10.1016/j.solener.2016.11.030.

Abal, G., Monetta, A., & Alonso-Suárez, R. (2018). Outdoor solar radiometer calibration under iso-9847:1992 standard and alternative methods. In *2018 IEEE 9th Power, Instrumentation and Measurement Meeting (EPIM)* (pp. 1–6). doi:10.1109/EPIM.2018.8756376.

Badosa, J., Wood, J., Blanc, P., Long, C. N., Vuilleumier, L., Demengel, D., & Haeffelin, M. (2014). Solar irradiances measured using spn1 radiometers: uncertainties and clues for development. *Atmospheric Measurement Techniques*, *7*, 4267–4283. doi:10.5194/amt-7-4267-2014.

Batlles, F., Olmo, F., & Alados-Arboledas, L. (1995). On shadowband correction methods for diffuse irradiance measurements. *Solar Energy*, *54*, 105 – 114. doi:https://doi.org/10.1016/0038-092X(94)00115-T.

Brunger, A. P., & Hooper, F. C. (1993a). Anisotropic sky radiance model based on narrow field of view measurements of shortwave radiance. *Solar Energy*, *51*, 53 – 64. doi:https://doi.org/10.1016/0038-092X(93)90042-M.

Brunger, A. P., & Hooper, F. C. (1993b). Erratum to anisotropic sky radiance model based on narrow field of view measurements of shortwave radiance. *Solar Energy*, *51*, 523.

Drummond, A. J. (1956). On the measurement of sky radiation. *Archiv für Meteorologie, Geophysik und Bioklimatologie, Serie B*, *7*, 413 – 436. doi:https://doi.org/10.1007/BF02242969.

Gracia, A., Torres, J., Blas], M. D., García, A., & Perez, R. (2011). Comparison of four luminance and radiance angular distribution models for radiance estimation. *Solar Energy*, *85*, 2202 – 2216. doi:https://doi.org/10.1016/j.solener.2011.06.005.

Gueymard, C., & Ruiz-Arias, J. (2016). Extensive worldwide validation and climate sensitivity analysis of direct irradiance predictions from 1-min global irradiance. *Solar Energy*, *128*, 1–30.

Gueymard, C. A. (2014). A review of validation methodologies and statistical performance indicators for modeled solar radiation data: Towards a better bankability of solar projects. *Renewable and Sustainable Energy Reviews*, *39*, 1024 – 1034. doi:https://doi.org/10.1016/j.rser.2014.07.117.

Ineichen, P., Gremaud, J., Guisan, O., & Mermoud, A. (1984). Study of the corrective factor involved when measuring the diffuse solar radiation by use of the ring method. *Solar Energy*, *32*, 585 – 590. doi:https://doi.org/10.1016/0038-092X(84)90133-6.

Iqbal, M. (1983). *An introduction to solar radiation*. Academic Press.

Kasten, F., Dehne, K., & Brettschneider, W. (1983). Improvement of measurement of diffuse solar radiation. In W. Palz (Ed.), *Solar Radiation Data* (pp. 221–225). Dordrecht: Springer Netherlands.

Kipp & Zonen (2004). *CM121 Shadow Ring Instruction Manual*. Instruction Manual Kipp & Zonen B.V. www.kippzonen.com.

Kudish, A., & Ianetz, A. (1993). Analysis of diffuse radiation data for beer sheva: Measured (shadow ring) versus calculated (global-horizontal beam) values. *Solar Energy*, *51*, 495 – 503. doi:https://doi.org/10.1016/0038-092X(93)90134-A.

Kudish, A. I., & Evseev, E. G. (2008). The assessment of four different correction models applied to the diffuse radiation measured with a shadow ring using global and normal beam radiation measurements for beer sheva, israel. *Solar Energy*, *82*, 144 – 156. doi:https://doi.org/10.1016/j.solener.2007.06.006.

Laguarda, A., Giacosa, G., Alonso-Suárez, R., & Abal, G. (2020). Performance of the site-adapted cams database and locally adjusted cloud index models for estimating global solar horizontal irradiation over the pampa húmeda. *Solar Energy*, *199*, 295–307. doi:https://doi.org/10.1016/j.solener.2020.02.005.

LeBaron, B., Michalsky, J., & Perez, R. (1990). A simple procedure for correcting shadowband data for all sky conditions. *Solar Energy*, *44*, 249 – 256. doi:https://doi.org/10.1016/0038-092X(90)90053-F.

LeBaron, B. A., Peterson, W. A., & Dirmhirn, I. (1980). Corrections for diffuse irradiance measured with shadowbands. *Solar Energy*, *25*, 1 – 13. doi:https://doi.org/10.1016/0038-092X(80)90401-6.

López, G., Muneer, T., & Claywell, R. (2004). Assessment of four shadow band correction models using beam normal irradiance data from the united kingdom and israel. *Energy Conversion and Management*, *45*, 1963 – 1979. doi:https://doi.org/10.1016/j.enconman.2003.11.001.

Maxwell, E., Wilcox, S., & Rymes, M. (1993). *Users Manual for SERI QC Software: Assessing the Quality of Solar Radiation Data*. NREL/TP-463-5608 National Renewable Energy Laboratory.

McArthur, L. (2005). *Baseline Surface Radiation Network (BSRN) Operations Manual*. TD-No. 1274, WRCP/WMO World Meteorological Organization (WMO). www.wmo.org.

Moon, P., & Spencer, D. (1942). Illumination from a non-uniform sky. *Illum. Engng.(NY)*, *37*, 707–726.

Muneer, T. (1990). Solar Radiation Model for Europe . *Building Services Engineering Research and Technology*, *11*, 153–163. doi:https://doi.org/10.1177/014362449001100405.

Muneer, T., & Zhang, X. (2001). A New Method for Correcting Shadow Band Diffuse Irradiance Data . *Journal of Solar Energy Engineering*, *124*, 34–43. doi:https://doi.org/10.1115/1.1435647.

Painter, H. (1981). The shade ring correction for diffuse irradiance measurements. *Solar Energy*, *26*, 361 – 363. doi:https://doi.org/10.1016/0038-092X(81)90182-1.

Peel, M. C., Finlayson, B. L., & Mcmahon, T. A. (2007). Updated world map of the köppen-geiger climate classification. *Hydrology and Earth System Sciences Discussions*, *11*, 1633–1644.

Perez, R., Ineichen, P., Seals, R., Michalsky, J., & Stewart, R. (1990). Modeling daylight availability and irradiance components from direct and global irradiance. *Solar Energy*, *44*, 271 – 289. doi:https://doi.org/10.1016/0038-092X(90)90055-H.

Perez, R., Seals, R., & Michalsky, J. (1993). All-weather model for sky luminance distribution—preliminary configuration and validation. *Solar Energy*, *50*, 235 – 245. doi:https://doi.org/10.1016/0038-092X(93)90017-I.

Polo, J., Wilbert, S., Ruiz-Arias, J., Meyer, R., Gueymard, C., Súri, M., Martín, L., Mieslinger, T., Blanc, P., Grant, I., Boland, J., Ineichen, P., Remund, J., Escobar, R., Troccoli, A., Sengupta, M., Nielsen, K., Renne, D., Geuder, N., & Cebecauer, T. (2016). Preliminary survey on site-adaptation techniques for satellite-derived and reanalysis solar radiation datasets. *Solar Energy*, *132*, 25 – 37. doi:https://doi.org/10.1016/j.solener.2016.03.001.

Rawlins, F., & Readings, C. (1986). The shade ring correction for measurements of diffuse irradiance under clear skies. *Solar Energy*, *37*, 407 – 416. doi:https://doi.org/10.1016/0038-092X(86)90031-9.

Ridley, B., Boland, J., & Lauret, P. (2010). Modelling of diffuse solar fraction with multiple predictors. *Renewable Energy*, *35*, 478 – 483. doi:https://doi.org/10.1016/j.renene.2009.07.018.

Ruiz-Arias, J., Alsamamra, H., Tovar-Pescador, J., & Pozo-Vázquez, D. (2010). Proposal of a regressive model for the hourly diffuse solar radiation under all sky conditions. *Energy Conversion and Management*, *51*, 881 – 893. doi:https://doi.org/10.1016/j.enconman.2009.11.024.

de Simón-Martín, M., Díez-Mediavilla, M., & Alonso-Tristán, C. (2016). Shadow-band radiometer measurement of diffuse solar irradiance: Calculation of geometrical and total correction factors. *Solar Energy*, *139*, 85 – 99. doi:https://doi.org/10.1016/j.solener.2016.09.026.

Siren, K. (1987). The shadow band correction for diffuse irradiation based on a two-component sky radiance model. *Solar Energy*, *39*, 433 – 438. doi:https://doi.org/10.1016/S0038-092X(87)80062-2.

Stanhill, G. (1985). Observations of shade-ring corrections for diffuse sky radiation measurements at the dead sea. *Quarterly Journal of the Royal Meteorological Society*, *111*, 1125–1130. doi:10.1002/qj.49711147013.

Steven, M. D. (1984). The anisotropy of diffuse solar radiation determined from shade-ring measurements. *Quarterly Journal of the Royal Meteorological Society*, *110*, 261–270. doi:https://doi.org/10.1002/qj.49711046317.

Steven, M. D., & Unsworth, M. H. (1980). Shade-ring corrections for pyranometer measurements of diffuse solar radiation from cloudless skies. *Quarterly Journal of the Royal Meteorological Society*, *106*, 865–872. doi:10.1002/qj.49710645015.

Sánchez, G., Serrano, A., Cancillo, M. L., & García, J. A. (2012). Comparison of shadow-ring correction models for diffuse solar irradiance. *Journal of Geophysical Research: Atmospheres*, *117*. doi:10.1029/2011JD017346.

Vartiainen, E. (1999). An anisotropic shadow ring correction method for the horizontal diffuse irradiance measurements. *Renewable Energy*, *17*, 311–317. doi:10.1016/S0960-1481(98)007.

Vignola, F., Michalsky, J., & Stoffel, T. (2019). *Solar and Infrared Radiation Measurements https://www.taylorfrancis.com/books/9781315105130*.